

Bright, high repetition rate water window soft X-ray source enabled by nonlinear pulse self-compression in antiresonant hollow-core fibre

M. Gebhardt,^{1,2*} T. Heuermann,^{1,2} R. Klas,^{1,2} C. Liu,^{1,2} A. Kirsche,^{1,2} M. Lenski,¹ Z. Wang,¹ C. Gaida,¹⁺ J. E. Antonio-Lopez,³ A. Schülzgen,³ R. Amezcua-Correa,³ J. Rothhardt,^{1,2,4} and J. Limpert,^{1,2,4}

¹*Institute of Applied Physics, Abbe Center of Photonics, Friedrich-Schiller-Universität Jena, Albert-Einstein-Str. 15, 07745 Jena, Germany*

²*Helmholtz-Institute Jena, Fröbelstieg 3, 07743 Jena, Germany*

³*CREOL, College of Optics and Photonics, University of Central Florida, Orlando, Florida 32816, USA*

⁴*Fraunhofer Institute for Applied Optics and Precision Engineering, Albert-Einstein-Str. 7, 07745 Jena, Germany*

⁺*now with Active Fiber Systems GmbH, Ernst-Ruska-Ring 17, 07745 Jena, Germany*

*Corresponding author: martin.gebhardt@uni-jena.de

Bright, coherent soft X-ray (SXR) radiation is essential to a variety of applications in fundamental research and life sciences¹. So far, high photon flux in this spectral region can only be delivered by synchrotrons, free electron lasers or high-order harmonic generation (HHG) sources, which are driven by kHz-class repetition rate lasers with very high peak powers. Here, we establish a novel route toward powerful and easy-to-use SXR sources by presenting a compact experiment, in which nonlinear pulse self-compression to the few-cycle regime is combined with phase-matched HHG in a single, helium-filled antiresonant hollow-core fibre (ARHCF). This enables the first 100 kHz-class repetition rate, table-top SXR source, that delivers an application-relevant flux of 2.8×10^6 Photons/s/eV around 300 eV. The fibre-integration of temporal pulse self-compression (leading to the formation of the necessary strong-field waveforms) and pressure controlled phase-matching will allow compact, high repetition rate laser technology, including commercially available systems, to drive simple and cost-effective, coherent high-flux SXR sources.

Laser-driven SXR sources based on HHG² are known for their table-top dimensions, excellent spatial coherence and ultrashort pulse durations, which make them attractive tools for advanced spectroscopy^{3,4}. Additionally, they are expected to enable the area-wide evolution of lens-less imaging in the water window⁵, and they hold great promise for the production of isolated attosecond pulses shorter than the atomic unit of time^{6,7}.

In the past decade, water window HHG has mostly been achieved with the help of optical parametric amplifiers, operating around 2 μm wavelength^{4,8-11}. This driving wavelength is identified as a “sweet-spot” for pushing the phase-matched harmonic energy ($\sim \lambda^{1.4-1.7}$) beyond the carbon K-edge without sacrificing too much efficiency ($\sim \lambda^{-6.5}$)¹². To date, the reported generated photon flux around 300 eV is as high as 1×10^9 Photons/s/eV at 1 kHz repetition rate⁴. To achieve high flux levels, the typical experimental conditions require >40 GW peak power (Supplement), which implies the generation and handling of multi-mJ energy^{4,9}, or few-cycle pulses^{11,13}. These experimental constraints alter the fundamentally desired user-friendly and straightforward nature of laser-based SXR sources and they are responsible for the fact that subsequent work on applications is often closely related to source development^{4,11}. Additionally, techniques like coincidence detection¹⁴ and space-charge-reduced photoelectron spectroscopy¹⁵ require repetition rates >1 kHz, where generation and handling of high peak power pulses become increasingly challenging and the reported 300 eV flux is only around 4×10^4 Photons/s/eV^{9,13}. It is therefore highly desired to enable compact, high repetition rate laser sources (including turnkey, commercial systems) to directly generate high-flux SXR high-order harmonics.

In this work, we demonstrate an approach to SXR HHG, which is based on power-scalable laser emission from a 98 kHz repetition rate thulium-doped fibre laser. It combines nonlinear self-compression of the driving pulses¹⁶ with waveguide HHG¹⁷ within a single, gas-filled ARHCF. The fibre-integrated HHG experiments require only GW-level peak power, multi-cycle laser pulses as a result of the carefully controlled intensity enhancement during the pulse compression. While so-called all-fibre, table-top SXR sources, driven by

mid-infrared lasers, have been briefly envisaged theoretically¹⁸, it is the first time that this scheme is experimentally realized and analysed in depth. This is fundamentally enabled by advances in the development of ARHCFs¹⁹ and represents a significant step in increasing the availability and performance of high repetition rate sources for SXR or attosecond science.

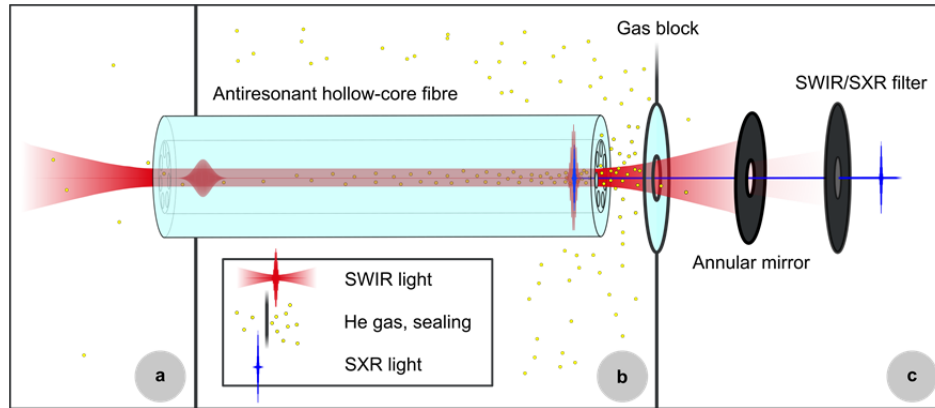


Fig. 1 Nonlinear pulse self-compression and HHG setup. **a**, Input coupling within helium gas at atmospheric pressure. **b**, The ARHCF (core diameter: 84.5 μm , length: 120 cm) is differentially pumped with the output facet located in a high-pressure chamber. Near the fibre output, the high-pressure region is separated from the following vacuum chamber by a 1 mm thick sapphire window that has a conical hole with diameters 100 μm to 250 μm . This gas block prevents most of the helium from reaching the following low-pressure region, while the light emerging from the fibre passes through. To achieve this, the ARHCF output (located approximately 2 mm away from the gas block) is movable in the horizontal and vertical direction (only the optimal positioning is shown for clarity). **c**, The final vacuum chamber contains an annular mirror, a thin metal filter to separate the SWIR light from the generated high-order harmonics, and a flat-field imaging grating spectrometer (not shown).

Our experiments are enabled by a thulium-doped fibre chirped-pulse amplification system, that provides 100 fs-pulses with energies up to 450 μJ , at a central wavelength of 1910 nm (Methods, Supplement). To prevent absorption from water vapor or thermal failure of the fibre tip²⁰, the mode coupling to the ARHCF is performed within helium gas at 1 bar pressure (Fig. 1a). From its output end, the fibre can be filled with helium at a pressure of up to 20 bar. Even at this pressure, the zero-dispersion wavelength is below the central wavelength of the laser pulses (Methods). Hence, those pulses self-compress as they undergo self-phase modulation while propagating to the output of the waveguide. For appropriately chosen input pulse energy and output pressure, the enhanced electric field strength close to the fibre end is high enough to directly drive HHG within the ARHCF (Fig. 1b). We note that the typical phase-matched photon energy cut-off achieved with short-wavelength infrared (SWIR) driving wavelengths is in the SXR regime¹². Because of the good transparency of helium in that spectral region, the high photon energy portion of the generated harmonics is well-transmitted to the characterization (Fig. 1c) or to subsequent experiments.

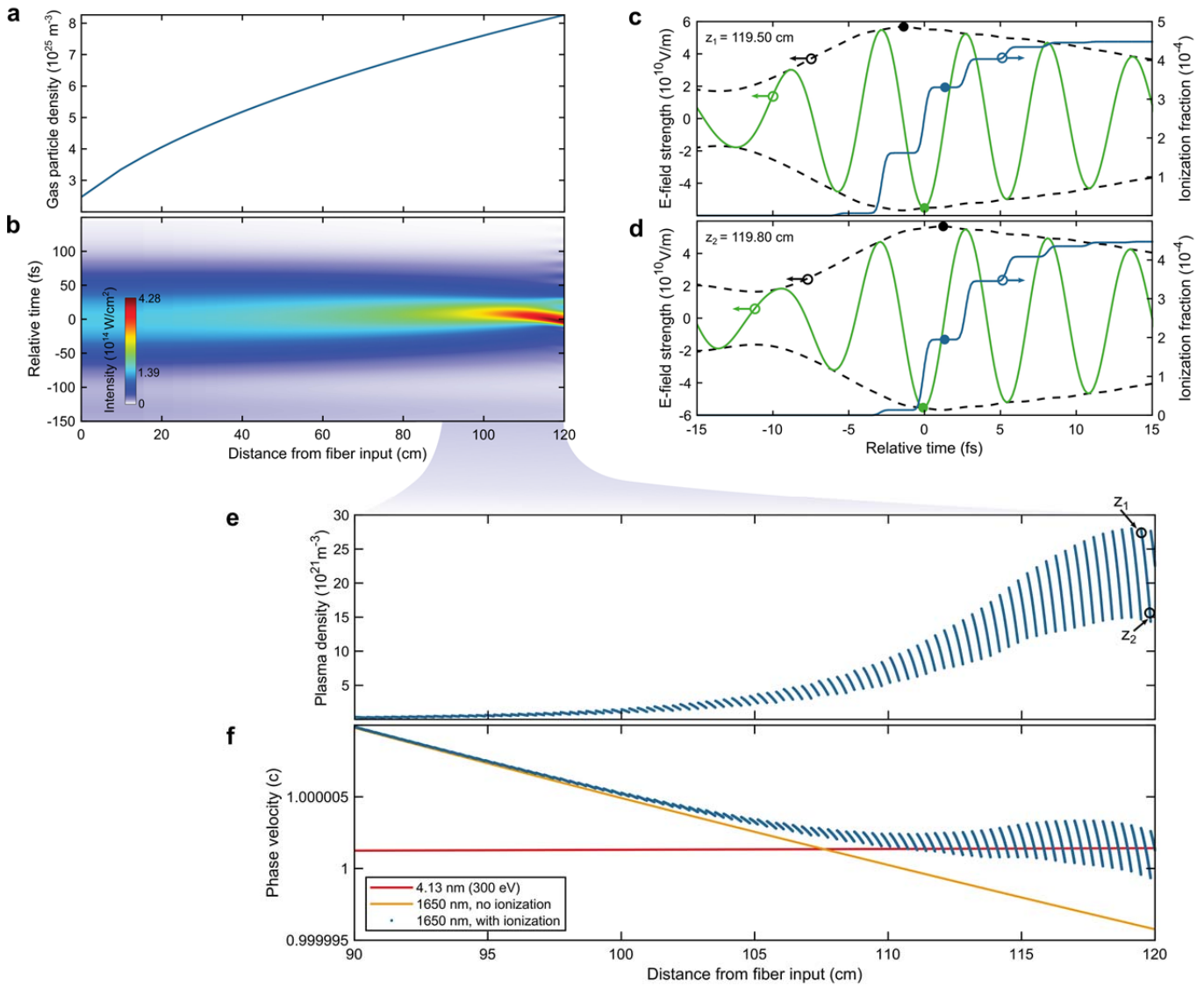


Fig. 2 Nonlinear pulse self-compression and simultaneous phase-matching of SWIR and SXR. **a**, Helium gas particle density along the fibre for pressures of 1 bar at the input and 3.345 bar at the output. **b**, Evolution of the simulated time dependent on-axis intensity within the fibre. The reference frame velocity is the group velocity at 1910 nm. **c**, Simulated time dependent electric field strength (green line), envelope (black dashed line) and ionization fraction (blue line) at a distance $z_1=119.50 \text{ cm}$ from the fibre input. Solid points highlight the field peak values/positions and the ionization fraction after the global peak of the electric field. The relative time axis is centred at the electric field maximum at z_1 . **d**, same as **c**, but at $z_2=119.80 \text{ cm}$ from the fibre input. The reference frame velocity is the phase velocity at 1650 nm. **e**, Simulated on-axis plasma density after the global peak of the electric field. **f**, Comparison of the SWIR and SXR phase velocities vs. distance from the fibre input.

A numerical analysis of the pulse self-compression (Methods) and phase-matching to the SXR is presented in Fig. 2. The input pulse characteristics are chosen to represent experimental conditions (Supplement). The steady state gas particle density within the ARHCF (Fig. 2a) is retrieved from gas flow modelling (Methods), with a pressure of 3.345 bar at the fibre output. Fig. 2b shows the evolution of the time dependent on-axis intensity inside of the fibre for a launch pulse energy of 265 μJ . The nonlinear dynamics cause the pulses to self-compress from initially 100 fs FWHM duration to below 20 fs (3.5 optical cycles) as they reach a position just before the fibre output. At this point, the peak intensity is increased to $4.28 \times 10^{14} \text{ W/cm}^2$, which causes ionization of the gas as can be seen from the acceleration of the pulse (Fig. 2b)²¹. To observe a significant growth of harmonic radiation, it is required to fulfil the phase-matching conditions² for at least one half-cycle within the SWIR pulse. Due to the significant field strength dependence of the atomic response²² and temporal walk-off effects²³, phase-matching close to the centre of the driving pulse is preferred. Consequently, we evaluate the ionization levels directly after the peak of the pulse. For example, Fig. 2c shows the simulated time dependent electric field and ionization fraction at a distance $z_1=119.50 \text{ cm}$. This is compared to the situation at $z_2=119.80 \text{ cm}$ (Fig. 2d). It becomes apparent that the evolution of the on-axis plasma density directly after the global electric field maximum (Fig. 2e) exhibits a modulation due to the temporal walk-off between the carrier and its envelope. This walk-off is a direct consequence of the waveguide dispersion, like the Gouy phase shift in tight focusing geometry. It can furthermore be derived from the self-compressed electric fields that the instantaneous wavelength of the most intense cycle is about 1650 nm. This is not surprising as ionization causes a blue-shift of the spectrum²¹. Finally, the above derived quantities are used to calculate the phase velocities for the centre of the HHG driving pulse and a desired high-order harmonic wavelength. It can be seen in Fig. 2f, that the chosen output pressure is not only crucial for the intensity enhancement achieved through pulse self-compression. Most importantly, it counteracts the ionization-induced acceleration of the driving field's phase velocity such that it travels in phase with the generated SXR light over a macroscopic distance.

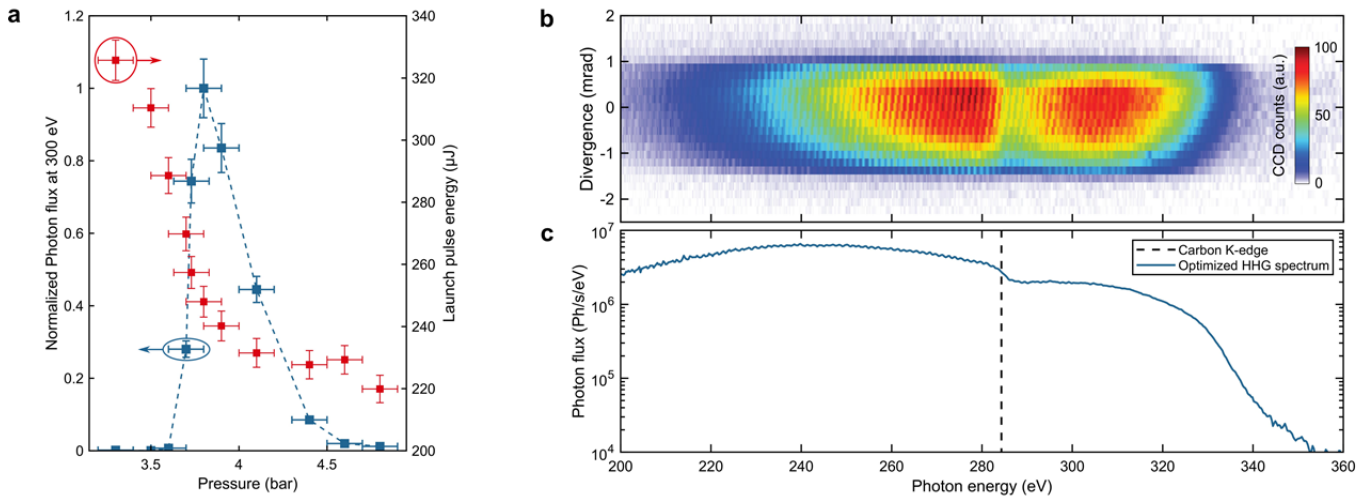


Fig. 3 High-harmonic generation experimental results. **a**, Normalized generated photon flux, evaluated at 300 eV for different helium gas pressures applied to the high-pressure chamber. The individual error bars in the y-direction are based on a standard deviation of 240 consecutive measurements (Supplement) and the uncertainty of the pressure reading (0.1 bar). Measured flux data points are connected by the blue dashed line. The right y-axis refers to the launch pulse energy necessary for obtaining optimum flux at each pressure setting. **b**, Measured HHG spectrum and divergence for optimized experimental conditions. The clipping in the divergence direction is due to the limited apertures of the SWIR/SXR separation elements. **c**, Evaluation of the generated photon flux, not accounting for carbon contaminations as can be seen from the K-edge absorption feature at 284 eV photon energy.

The experimental conditions are optimized with the goal to generate high photon flux around 300 eV. This is done by scanning the gas pressure applied to the high-pressure chamber and subsequently adjusting the launch pulse energy for optimum flux (Fig. 3a). It is found that the optimization parameter exhibits a sharp peak around a pressure of 3.8 bar, which agrees reasonably well with the expectations from our numerical analysis (Fig. 2). A drop in flux to $\sim 1/e^2$ -times the optimum value is observed for a relative pressure change of 10%. In contrast to this, the pulse propagation simulations show that the overall nonlinearity of the pulse self-compression and, consequently, the peak electric field strength at the fibre output are easily restored when adjusting the launch pulse energy to a 10% pressure change. Therefore, we conclude that controlling the gas pressure allows for controlling the phase-matching and for favouring the coherent growth of SXR light in the ARHCF. Fig. 3b presents a measured HHG spectrum including the beam divergence, which is represented on the vertical axis. For the signal-optimized experimental conditions, a full-angle divergence of about 2 mrad (Methods) and a phase-matched photon energy cut-off around 330 eV is observed. In fact, the simulated, phase-matched half-cycle cut-off is 334 eV (Supplement). In the experiment presented herein, an overall flux of $(2.8 \pm 1.8) \times 10^6$ Photons/s/eV is generated at 300 eV (Fig. 3c, Methods). Using only one annular mirror and one 200 nm thin aluminium filter, the SWIR suppression is $>10^6$, with $(1.3 \pm 0.8) \times 10^5$ Photons/s/eV available for experiments. To show that this is the first time, that a table-top 100 kHz-class repetition rate source delivers an application-relevant flux in the water window, we demonstrate X-ray

absorption fine-structure spectroscopy near the carbon K-edge and we measure an integrated power RMS stability <5% in the water window over 20 minutes (Supplement).

In conclusion, we have demonstrated nonlinear pulse self-compression and SXR HHG at 98 kHz repetition rate in a single ARHCF. This results in $>10^6$ Photons/s/eV at 300 eV, directly emitted from the fibre output. It is the first time that such an experiment is reported and its results show that high repetition rate ultrafast lasers, which deliver moderate pulse peak powers, can be used in a simple, integrated scheme to generate high-order harmonics up to the water window. Because the SXR yield is not absorption-limited, and the involved ionization levels are below the critical limit for phase-matching, we see significant prospects for advancing the approach described herein in terms of photon flux (Supplement). Furthermore, with an increase in driving laser wavelength²⁴, self-compression in ARHCFs will allow to directly generate keV photon energies and extremely short attosecond pulses at ≥ 100 kHz repetition rate.

While our work opens up possibilities to study complementary techniques like quasi phase-matching²⁵ or driving pulse synthesis²⁶ within the waveguide, we believe that its results are most interesting for a variety of applications, which significantly benefit from compact and easy-to-use high repetition rate SXR sources, e.g. coincidence spectroscopy¹⁴ or table-top lens-less imaging of organic samples⁵. Because of the versatility of the pulse self-compression, this approach can be scaled to much higher peak powers¹⁶. However, we believe that this work represents, first and foremost, a milestone in the development of industrial grade, laser-driven SXR sources. These sources could use ARHCFs for beam delivery²⁷, self-compression and HHG in a single apparatus, making them more affordable, and available to a much broader community in fundamental and applied sciences with medical applications in reach.

Methods

Fibre laser setup

The ultrafast fibre laser system is seeded by a commercial seed source and uses thulium-doped photonic crystal fibres within the first preamplification stages. The pulses are stretched to a duration of about 1 ns using a grating-based, Oeffner-type stretcher before further amplification and reduction of the oscillator repetition rate based on an acousto-optic modulator. The pulse train of 98 kHz repetition rate has an average power of approximately 200 mW prior to the main amplifier of the system that consists of a thulium-doped large-pitch fibre with a core diameter of 80 μm . The main amplifier is pumped with a commercially available 793 nm diode laser and increases the average power to about 50 W. After the pulse compression in a grating-based Treacy-type compressor, that is enclosed in a vacuum chamber, the output pulses carry up to 450 μJ of energy and have a duration (FWHM) of 100 fs.

Dispersion of ARHCF

The dispersion of the ARHCF is modelled as described in ref.¹⁸. The fibre used in the experiments described herein has a resonance band up to a wavelength of 1380 nm. This resonance is accounted for by an additional term added to the propagation constant²⁸, which we use for the pulse propagation simulations. We find the zero-dispersion wavelength (<700 nm in this case) by numerically calculating the root of the group velocity dispersion.

Calculation of gas flow and gas density

The gas flow through the ARHCF is modelled as described in²⁹, assuming a circular tube with 84.5 μm diameter and 120 cm length. It can be shown that the continuum component of the flow dominates strongly over the molecular flow component, allowing us to use the well-known description for the pressure and density distribution³⁰

$$p(z) = \sqrt{p_0^2 + \frac{z}{L}(p_L^2 - p_0^2)}$$

where p_L and p_0 are the fixed pressures at $z = L$, the fibre output, and $z = 0$, the fibre input.

Simulation of pulse propagation

The numerical simulations of the pulse propagation in the fibre were performed based on the unidirectional field propagation equation for the fundamental mode³¹:

$$\partial_z E(z, \omega) = i \left(\beta(\omega) - \frac{\omega}{v} \right) E(z, \omega) + i \frac{\omega^2}{2c^2 \epsilon_0 \beta(\omega)} P^{NL}(z, \omega)$$

Here, E is the electric field amplitude in the spectral domain, ω is the angular frequency, β is the fundamental mode propagation constant, v is the reference frame velocity, c is the vacuum speed of light, ϵ_0 is the Vacuum permittivity and P^{NL} is the nonlinear polarization. P^{NL} is influenced by the Kerr-nonlinearity and plasma formation, which we include in the simulations by calculating the Amossov-Delone-Krainov ionization rates³².

Calculation of phase velocities

The phase velocity of the high-order harmonics has been calculated from the refractive index data available in ref.³³. For the driving field's propagation constant, which gives straightforward access to its phase velocity, we made the approximation as described in²:

$$\beta(\omega) = \frac{\omega}{c} \cdot \left(1 + \frac{p}{p_0} (1 - \eta) \cdot \delta \right) - \frac{2\pi c}{\omega} \cdot \left(\frac{p}{p_0} \eta N_{atm} r_e + \frac{2.4048^2}{4\pi a^2} \right)$$

where p and p_0 are the pressure and the experimental pressure at standard conditions, η is the ionization fraction, δ is the neutral gas dispersion, N_{atm} is the number density at standard conditions, r_e is the classical electron radius and a is the core radius of the hollow fiber (see Supplement for definition).

Determination of launch pulse energy

In low power operation, the overall transmission of the 120 cm long ARHCF was about 90%. During the HHG experiments, we have performed a relative power monitoring of the output power, which was used together with the simulation results to determine the experimental launch pulse energy as shown in figure 3a. This gives 86% transmission for the experimental conditions of optimal HHG signal (see table S1).

Characterization of HHG flux

The photon flux is estimated from the spectral characterization of the HHG signal. This method is discussed in more detail in ref.³⁴, where the flux in photons per second, $N_{ph,s}$, is given as:

$$N_{ph,s} = \frac{S_{CCD} \cdot \sigma}{\eta_{QE} \cdot E_{ph}^{[bg]} \cdot \eta_g \cdot t_f \cdot t_{gas} \cdot t_{exp}}$$

Here, S_{CCD} is the measured signal (counts) on the detector, σ and η_{QE} are the CCD sensitivity and the CCD quantum efficiency, $E_{ph}^{[bg]}$ is the evaluated HHG photon energy in units of a bandgap energy of 3.65 eV. The factor $\sigma / (\eta_{QE} \cdot E_{ph}^{[bg]})$ was calibrated for the CCD in use by the Physikalisch-Technische Bundesanstalt (PTB). η_g is the grating diffraction efficiency (retrieved from measurements

using free-electron-laser radiation³⁵), t_f is the transmission of the used 200 nm aluminum filter (which is measured experimentally), t_{gas} is the theoretical transmission through the helium gas, consisting of the high pressure region (see main text) and the low pressure spectrometer chamber, for which we determine a propagation length of 1.25 m and a pressure of 0.7 mbar. Finally, t_{exp} is the exposure time of the measurement. In addition to these corrections, the clipping of the HHG beam, as can be seen in figure 3b, is corrected. For this purpose, a Gaussian profile is fitted to the vertical outline of the signal at 300 eV. This evaluation also gives an estimated full divergence angle of 2 mrad. The combined relative uncertainties of the quantities mentioned above give a worst-case error estimation of $\pm 64\%$ for the absolute flux value.

The visible dip at around 284 eV (figure 3b and 3c) is associated with the K-shell absorption in carbon and relates to a 35 nm hydrocarbon film, that is most likely deposited on the spectrometer grating.

Acknowledgements

The authors would like to thank Prof. Adrian Pfeiffer and Dr. Felix Köttig for fruitful discussions and help with the numerical methods. Furthermore, the authors would like to thank Dr. Steffen Hädrich, Dr. Cesar Jauregui-Misas and Tobias Ulsperger for their help in the early stages of this work.

This work was supported by the European Research Council (ERC) under the European Union's Horizon 2020 research and innovation programme (grant 835306, SALT), the Fraunhofer Cluster of Excellence Advanced PhotonSources (CAPS), the Helmholtz-Institute Jena, the U.S. Army Research Office (grant W911NF1910426) and the U.S. Airforce Office of Scientific Research (grant FA9550-15-10041).

Author contributions

J.L., J.R., M.G. and R.K. conceived and planned the experiment. The ultrafast fibre laser and the nonlinear pulse compression stage were built and optimised by M.G., T.H., M.L., Z.W and C.G. The antiresonant hollow-core fibre was designed and drawn by J.A.-L., A.S. and R.A.-C. The HHG experiments were performed by M.G., T.H., R.K., C.L. and A.K. Simulations and data analysis were performed by

M.G. with support from T.H. and R.K. All authors discussed and contributed to the interpretation of the results and to the writing of the manuscript. J.L. and J.R. supervised the project, J.L., R.A.-C and J.R. acquired funding.

Competing interests

The authors declare no competing interests.

References

1. Young, L. *et al.* Roadmap of ultrafast x-ray atomic and molecular physics. *J. Phys. B At. Mol. Opt. Phys.* **51**, 032003 (2018).
2. Rundquist, A. *et al.* Phase-Matched Generation of Coherent Soft X-rays. *Science (80-.)*. **280**, 1412–1415 (1998).
3. Pertot, Y. *et al.* Time-resolved x-ray absorption spectroscopy with a water window high-harmonic source. *Science (80-.)*. **267**, 264–267 (2017).
4. Popmintchev, D. *et al.* Near- and Extended-Edge X-Ray-Absorption Fine-Structure Spectroscopy Using Ultrafast Coherent High-Order Harmonic Supercontinua. *Phys. Rev. Lett.* **120**, 093002 (2018).
5. Rose, M. *et al.* Quantitative ptychographic bio-imaging in the water window. *Opt. Express* **26**, 1237 (2018).
6. Gaumnitz, T. *et al.* Streaking of 43-attosecond soft-X-ray pulses generated by a passively CEP-stable mid-infrared driver. *Opt. Express* **25**, 27506 (2017).
7. Li, J. *et al.* 53-attosecond X-ray pulses reach the carbon K-edge. *Nat. Commun.* **8**, 186 (2017).
8. Stein, G. J., Keathley, P. D., Krogen, P. & Liang, H. Water-window soft x-ray high-harmonic generation up to the nitrogen K-edge driven by a kHz, 2.1 μm OPCPA source. *J. Phys. B At. Mol. Opt. Phys.* **49**, 1–8.
9. Feng, T. *et al.* 27 W 21 μm OPCPA system for coherent soft X-ray generation operating at 10 kHz. *Opt. Express* **28**, 8724 (2020).
10. Johnson, A. S. *et al.* High-flux soft x-ray harmonic generation from ionization-shaped few-cycle laser pulses. *Sci. Adv.* **4**, eaar3761 (2018).
11. Cousin, S. L. *et al.* High-flux table-top soft x-ray source driven by sub-2-cycle, CEP stable, 185- μm 1-kHz pulses for carbon K-edge spectroscopy. *Opt. Lett.* **39**, 5383 (2014).
12. Chen, M.-C. *et al.* Bright, Coherent, Ultrafast Soft X-Ray Harmonics Spanning the Water Window from a Tabletop Light Source. *Phys. Rev. Lett.* **105**, 173901 (2010).
13. Pupekis, J. *et al.* Water window soft x-ray source enabled by a 25 W few-cycle 22 μm OPCPA at 100 kHz. *Optica* **7**, 168 (2020).
14. Rothhardt, J. *et al.* High-repetition-rate and high-photon-flux 70 eV high-harmonic source for coincidence ion imaging of gas-phase molecules. *Opt. Express* **24**, 18133 (2016).
15. Chiang, C.-T. *et al.* Boosting laboratory photoelectron spectroscopy by megahertz high-order harmonics. *New J. Phys.* **17**, 013035 (2015).
16. Travers, J. C., Grigorova, T. F., Brahms, C. & Belli, F. High-energy pulse self-compression and ultraviolet generation through soliton dynamics in hollow capillary fibres. *Nat. Photonics* **13**, 547–554 (2019).
17. Schnürer, M. *et al.* Guiding and high-harmonic generation of sub-10-fs pulses in hollow-core fibers at 1015 W/cm². *Appl. Phys. B Lasers Opt.* **67**, 263–266 (1998).
18. Travers, J., Chang, W., Nold, J., Joly, N. & Russell, P. S. J. Ultrafast nonlinear optics in gas-filled hollow-core photonic crystal fibers. *JOSA B* **28**, (2011).
19. Yu, F. & Knight, J. C. Negative Curvature Hollow-Core Optical Fiber. *IEEE J. Sel. Top. Quantum Electron.* **22**, 146–155 (2016).
20. Gebhardt, M. *et al.* Nonlinear pulse compression to 43 W GW-class few-cycle pulses at 2 μm wavelength. *Opt. Lett.* **42**, 4179 (2017).
21. Saleh, M. F. *et al.* Theory of Photoionization-Induced Blueshift of Ultrashort Solitons in Gas-Filled Hollow-Core Photonic Crystal Fibers. *Phys. Rev. Lett.* **107**, 203902 (2011).
22. Kazamias, S. *et al.* Pressure-induced phase matching in high-order harmonic generation. *Phys. Rev. A* **83**, 063405 (2011).
23. Hernández-García, C. *et al.* Group velocity matching in high-order harmonic generation driven by mid-infrared lasers. *New J. Phys.* **18**, 073031 (2016).
24. Elu, U. *et al.* High average power and single-cycle pulses from a mid-IR optical parametric chirped pulse amplifier. *Optica* **4**, 1024 (2017).
25. Wiegandt, F. *et al.* Quasi-phase-matched high-harmonic generation in gas-filled hollow-core photonic crystal fiber. *Optica* **6**, 442 (2019).
26. Jin, C., Wang, G., Wei, H., Le, A.-T. & Lin, C. D. Waveforms for optimal sub-keV high-order harmonics with synthesized two- or three-colour laser fields. *Nat. Commun.* **5**, 4003 (2014).
27. Michieletto, M. *et al.* Hollow-core fibers for high power pulse delivery. *Opt. Express* **24**, 7103 (2016).
28. Tani, F., Köttig, F., Novoa, D., Keding, R. & Russell, P. S. J. Effect of anti-crossings with cladding resonances on ultrafast nonlinear dynamics in gas-filled photonic crystal fibers. *Photonics Res.* **6**, 84 (2018).
29. Livesey, R. G. Solution methods for gas flow in ducts through the whole pressure regime. *Vacuum* **76**, 101–107 (2004).
30. Henningsen, J. & Hald, J. Dynamics of gas flow in hollow core photonic bandgap fibers. *Appl. Opt.* **47**, 2790 (2008).
31. Tani, F., Travers, J. C. & St.J. Russell, P. Multimode ultrafast nonlinear optics in optical waveguides: numerical modeling and

- experiments in kagomé photonic-crystal fiber. *J. Opt. Soc. Am. B* **31**, 311 (2014).
32. M. V. Ammosov, N. B. Delone, and V. P. K. Tunnel ionization of complex atoms and of atomic ions in an alternating electromagnetic field. *Sov. Phys. JETP* **64**, 4-7 (1986).
 33. Henke, B. L., Gullikson, E. M. & Davis, J. C. X-Ray Interactions: Photoabsorption, Scattering, Transmission, and Reflection at E = 50-30,000 eV, Z = 1-92. *At. Data Nucl. Data Tables* **54**, 181-342 (1993).
 34. Hädrich, S. *et al.* High photon flux table-top coherent extreme-ultraviolet source. *Nat. Photonics* **8**, 779-783 (2014).
 35. Frassetto, F. *et al.* Compact spectrometer for the analysis of high harmonics content of extreme-ultraviolet free-electron-laser radiation. in *Advances in X-Ray/EUV Optics and Components V* (eds. Khounsary, A. M., Morawe, C. & Goto, S.) vol. 7802 780209 (2010).